

ARTICLE OPEN



Unveiling multipole physics and frustration of icosahedral magnetic quasicrystals

Junmo Jeon¹ and SungBin Lee¹✉

Multipolar physics and their hidden orders have been widely discussed in the context of heavy fermions and frustrated magnets. However, despite extensive research, there are few examples of purely multipolar systems in the absence of magnetic dipoles. Here, we show the magnetic behavior of an icosahedral quasicrystal is generally described by multipoles, and in a specific case by pure magnetic octupoles, resulting from the interplay of spin-orbit coupling and crystal field splitting. Importantly, we emphasize that non-crystallographic symmetries of quasicrystals result in multipolar degrees of freedom, in contrast to the conventional crystals. We first classify the characteristics of multipoles and derive the effective spin Hamiltonian. We then explore how frustration and quantum fluctuations induce entangled quantum phases. Our study presents the magnetic icosahedral quasicrystal as a platform for investigating the exotic multipolar physics.

npj Quantum Materials (2024)9:5; <https://doi.org/10.1038/s41535-023-00617-z>

INTRODUCTION

Several examples in condensed matter systems are not easily observable through conventional experimental techniques. Such hidden orders have been in debate for several decades and have been waiting to be discovered^{1–7}. In particular, unusual higher rank multipole moments, beyond the conventional electric and magnetic dipole moments, have been suggested as a key player to exhibit various hidden orders^{8–33}. Multipolar degrees of freedom are renowned for not only generating hidden orders, but also contributing to a range of other intriguing and intricate phenomena. For example, in heavy fermion materials, multipolar degrees of freedom can lead to the emergence of unconventional superconductivity and non-Fermi liquid behavior with exotic Kondo physics^{34–45}. In addition, exotic ground states, known as multipolar quantum spin liquids, can emerge from the magnetic frustration between the multipolar moments^{46–49}. Therefore, the investigation of multipolar physics properties has been the primary objective of extensive research with significant implications and fresh insights that could potentially lead to various applications^{50–56}. However, there are few such examples, and many of the magnetic systems contain not only multipoles but also magnetic dipoles at the same time.

Finding multipolar degrees of freedom in the magnetic systems requires a delicate combination of spin-orbit couplings and crystalline electric field (CEF) splitting based on the point group symmetries^{33,57–59}. In conventional crystals, the point group symmetry, which should be compatible with the translational symmetry, limits the exploration of pure multipolar degrees of freedom in the magnetic systems⁵⁷. On the other hand, the quasicrystals, and their approximants could exhibit the point group symmetries beyond the space group such as pentagonal rotational symmetry, due to their ordered structure lacking spatial periodicity^{60–62}. Thus, quasicrystalline materials provide a good platform for finding multipolar degrees. Several rare-earth magnetic quasicrystals exhibit icosahedral symmetry, but their multipolar physics and related exotic phenomena have yet to be investigated^{63–68}.

In this paper, we consider the non-crystallographic 5-fold rotational symmetry and icosahedral symmetry with f-orbital electrons of the rare earth atoms. First, we classify all possible multipole degrees of freedom found in rare-earth magnetic quasicrystals in the presence of noncrystallographic 5-fold symmetry. We note that this generally leads to the higher order multipoles of the pseudospin x and y components, and magnetic dipoles of the Ising moments. More interestingly, if magnetic quasicrystals with Yb^{3+} ions are in a perfect icosahedral crystal field symmetry, they host the Kramers doublet that carries pure magnetic octupole moments without magnetic dipole moments. On symmetry grounds, the generic spin Hamiltonian is introduced for both Kramers and non-Kramers doublet. In the antiferromagnetic Ising limit, we first discuss the degenerate ground state resulting from the geometrically frustrated icosahedron structure. Subsequently, with the introduction of quantum fluctuations, a distinctive ground state is established, which has non-zero entanglement. In this case, depending on (anti-) ferromagnetic XY interaction, the specific linear combination of the degenerate ground states found in the Ising limit becomes a non-degenerate ground state. Our work provides a perspective for finding multipolar degrees of freedom and their magnetic frustration originated from noncrystallographic symmetries. Furthermore, it opens a paradigm for enriching hidden orders, spin liquids and Kondo effects in quasicrystals.

RESULTS

Multipolar degrees of freedom in icosahedral magnetic quasicrystals

In this section, we begin by categorizing all potential multipolar degrees of freedom for rare-earth magnetic systems with noncrystallographic 5-fold symmetry and icosahedral symmetry. We then shift our attention to a scenario wherein magnetic dipoles are absent, and pure magnetic octupole moments are present. We examine the characteristics of such moments.

¹Physics Department, Korea Advanced Institute of Science and Technology, Daejeon 34141, South Korea. ✉email: sungbin@kaist.ac.kr

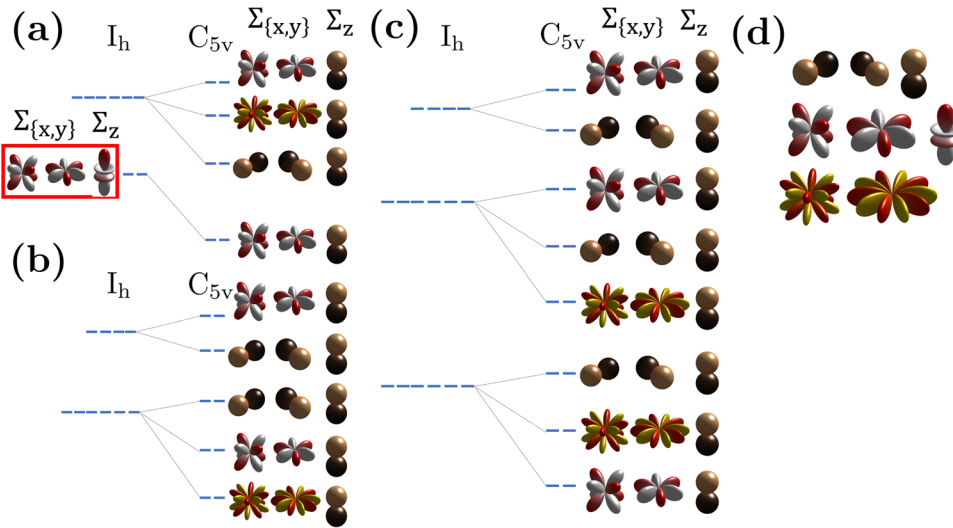


Fig. 1 Summary of the CEF states and multipoles under non-crystallographic point group symmetries for given half-integer values of J . **a** $J = 7/2$ (Yb^{3+}) **(b)** $J = 9/2$ (Nd^{3+}) and **(c)** $J = 15/2$ (Dy^{3+}). Under the icosahedral symmetry I_h , the CEF states are split into several multiplets. Particularly, note that $J = 7/2$ which is the case for Yb^{3+} has a Kramers doublet and it hosts pure magnetic octupoles without magnetic dipoles or quadrupoles, as shown in the red box. Whereas, for C_{5v} where the mirror reflection of I_h is absent, all the multiplets are split into Kramers doublets. In this case, the z -component of the pseudospin, Σ_z is dipole for any Kramers doublets. In contrast, the x, y -components, $\Sigma_{x,y}$, could be not only dipoles but also octupoles and dotriacontapoles. Depending on the energy scale of the breaking of the mirror symmetry, the order of energy could change. **d** Dipoles (black-copper), octupoles (red-white) and dotriacontapoles (red-yellow). See the main text for more details.

The most general CEF Hamiltonian in a 5-fold rotational symmetry is given as follows, using the Stevens operators,

$$H_{\text{CEF}} = B_{60}O_6^0 + B_{65}O_6^5 + B_{20}O_2^0 + B_{40}O_4^0 \quad (1)$$

Here, $B_{nm} = -\gamma_{nm}qC_{nm}\langle r^n \rangle \theta_n$ are the Stevens coefficients obtained by the radial integrals, where γ_{nm} is a term calculated from the ligand environment expressed in terms of tesseral harmonics. q is the charge of the central atom, C_{nm} are the normalization factors of the spherical harmonics, r is the radial position, θ_n are constants associated with electron orbitals of the magnetic ion⁶⁹. Here, we assume the point charge model. We neglect the finite extent of the charges on the ions, the overlap of the wave functions of the magnetic ions with those of neighboring ions, and the complex effects of the screening of the magnetic electrons by the outer electron shells of the magnetic ion. Nevertheless, we emphasize that it serves as a first approximation to illustrate the principles involved, and can be used to calculate the ratios of terms of the same degree in the Hamiltonian for lattice sites of high symmetry, since these ratios are independent of the models and are determined solely on symmetry grounds⁷⁰. Note that the z -axis is a 5-fold rotational symmetry axis. The O_n^m are Stevens operators with respect to the total angular momentum operators (See Supplementary Methods for the detailed forms of O_n^m). When we consider the full icosahedral symmetry, which has 5-fold rotational symmetry plus mirror reflection symmetries, it leads to $B_{20} = B_{40} = 0$, and $B_{65} = -42B_{60}$. We examine two cases one where perfect icosahedral symmetry exists, and another where only 5-fold symmetry exists. These cases are applicable to different situations. The latter case can be taken into account using the charge defects which breaks the icosahedral symmetry down to C_{5v} . In this case, the charge defect on a ligand is placed on a z -axis as $q \rightarrow q(1+a)$. As a result, the Stevens coefficients, B_{65}, B_{20}, B_{40} are changing as a function of a . Since $B_{nm} = -a\gamma'_{nm}qC_{nm}\langle r^n \rangle \theta_n$ for a single point charge defect, B_{60} is unchanged if the charge defect is placed on the z -axis. Most of the binary, ternary and complex Al-TM (TM = transition metal) icosahedral quasicrystals, similar to the Al-Mn or Al-Mn-Si compounds, belong to the Mackay-type of icosahedral quasicrystals which have perfect icosahedral

symmetry. In contrast, for instance, $\text{Ce}_{15}\text{Au}_{65}\text{Sn}_{20}$ has only C_{5v} point group symmetry around its magnetic atom, Ce^{61} .

For both full icosahedral symmetry, I_h and 5-fold rotational symmetry, C_{5v} with nonzero a , we summarize the CEF states in Figs. 1 and 2 for half-integer J and integer J values, respectively. For $a = 0$, the point group symmetry restores the full icosahedral symmetry and multiple degenerate levels appear. It is noteworthy that for $J = 7/2$ which is the case for Yb^{3+} , the (Kramers) doublet exists under the perfect icosahedral symmetry group as shown in the red box of Fig. 1a. Specifically, there are two eigenspaces of H_{CEF} , the Kramers doublet and the sextet⁷¹. On the other hand, for any given $a \neq 0$, the CEF states under 5-fold symmetry are split into doublets or singlets for all given values of the total angular momentum J of the rare earth atom. In both Figs. 1 and 2, the tentative orders of the energy levels are given for $a = 0.5$. Given $a \neq 0$, every energy levels for half-integer J are Kramers doublet due to the time-reversal symmetry. However, for integer J , some singlets are allowed. Notably, in all cases, the pseudospins of the doublets exhibit magnetic dipoles along the z -component, while typically showing multipoles such as quadrupoles, octupoles, and higher orders along the x and y -components. For half-integer values of J , $\Sigma_{x(y)}$ could be dipole, octupole and dotriacontapole (see Fig. 1), whereas for integer values of J , the doublets carry either quadrupole or hexadecapole $\Sigma_{x(y)}$ (see Fig. 2). Again, it is because of the time-reversal symmetry. It is interesting to note that for the low lying Kramers doublet, $\Sigma_{x(y)}$ for $J = 7/2$ always represents magnetic octupoles originated from the Kramers doublet, whereas, $\Sigma_{x(y)}$ for $J = 9/2$ and $J = 15/2$ could take magnetic octupoles or dotriacontapoles. We also note that for the low lying non-Kramers doublets, $\Sigma_{x(y)}$ for $J = 4$ and $J = 6$ take either quadrupole or hexadecapole, while for $J = 8$, it could take only quadrupole (see Fig. 2c).

We emphasize that the loss of translational symmetry generally allows such unconventional multipolar degrees of freedom. The aperiodic system allows the non-crystallographic point group symmetries which give rise to the unconventional terms of CEF Hamiltonian. For instance, 5-fold rotational symmetry leads to the O_6^5 term in Eq. (1). Note that the O_6^5 term relates $|J_z = m\rangle$ and

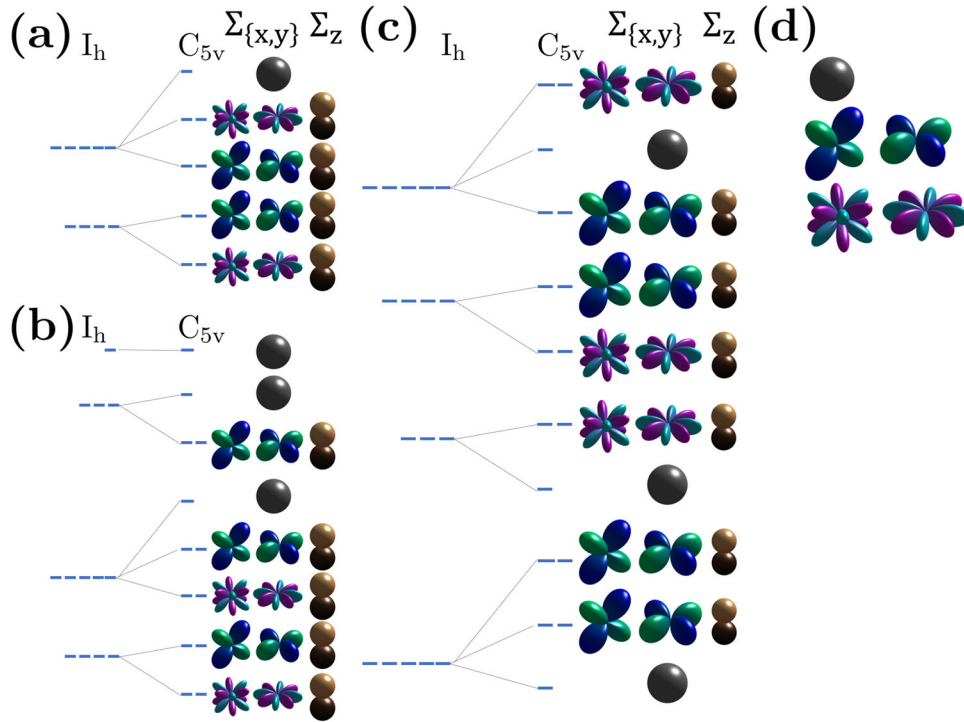


Fig. 2 Summary of the CEF states and multipoles under non-crystallographic point group symmetries for given integer values of J . **a** $J=4$ (Pr^{3+}) **(b)** $J=6$ (Tb^{3+}) and **(c)** $J=8$ (Ho^{3+}). Unlike the icosahedral symmetry I_h where the CEF states are split into several multiplets, the five-fold symmetry C_{5v} symmetry splits all the multiplets into either non-Kramers doublets or singlets. Under C_{5v} , the z-components of the pseudospin, Σ_z are magnetic dipoles for each doublet. On the other hand, the x,y-components, $\Sigma_{x,y}$ represent either quadrupoles or hexadecapoles. Depending on the energy scale of the breaking of mirror symmetry, the order of energy could change. **d** Singlet (black), quadrupoles (blue-skyblue) and hexadecapoles (violet-skyblue). See the main text for more details.

$|J_z = m \pm 5\rangle$ states, which are not related to each others in the conventional periodic systems. This allows us to obtain the multipolar degrees of freedom in the aperiodic system.

From now on, we focus on the special case where the lowest Kramers doublet is represented by pure octupoles, i.e. $J=7/2$ in an icosahedral crystal field symmetry and discuss their characteristics. Then, in the following subsections, we discuss the generic spin Hamiltonian, geometrical frustration and quantum fluctuation effects. It is important to note that all these arguments are generally applicable to any cases of multipolar physics with J listed in Figs. 1 and 2.

Let us define the Kramers doublet as $|\pm\rangle$, which are written in terms of the eigenstates of the J_z operator,

$$\begin{aligned} |+\rangle &= -\sqrt{\frac{7}{10}}|J_z = -\frac{3}{2}\rangle + \sqrt{\frac{3}{10}}|+\frac{7}{2}\rangle \\ |-\rangle &= \sqrt{\frac{3}{10}}|-\frac{7}{2}\rangle + \sqrt{\frac{7}{10}}|+\frac{3}{2}\rangle. \end{aligned} \quad (2)$$

With respect to the Yb^{3+} ion, it is established that $B_6 < 0$, thus the ground eigenspace of the CEF Hamiltonian is the Kramers doublet, which is well separated from the sextet^{72,73}. The CEF energy gap is given by $25200|B_{60}| \sim \mathcal{O}(10\text{meV})$, where detailed numerical value depends on icosahedral magnetic materials with Yb. Since the energy scale of spin exchanges between rare-earth ions are generally much smaller than the crystal field splittings, one can expect the magnetic properties at low temperature are explained within this Kramers doublet. From Eq. (2), one can easily find that $\langle \pm | J_i | \mp \rangle$ and $\langle \pm | J_i | \pm \rangle$ vanish where $i = x, y, z$. Importantly, J_z also vanishes due to the symmetric coefficients of the states. This confirms that there is no magnetic dipole moment. Thus, one should consider the multipolar degrees of freedom given by the irreducible tensor operators. However, since $|\pm\rangle$ are the Kramers doublet, the time-reversal even operators such as quadrupole moments vanish. Hence, it is reasonable to anticipate the

presence of higher-order degrees of freedom, such as octupoles, in the absence of dipolar or quadrupolar degrees of freedom.

To show that the Kramers doublet, $|\pm\rangle$ in Eq. (2), describes the octupolar degrees of freedom, let us define the pseudospin ladder operators, Σ^\pm , as follows.

$$\Sigma^+ = |+\rangle\langle -| \quad \Sigma^- = (\Sigma^+)^\dagger, \quad (3)$$

and $\Sigma^z = [\Sigma^+, \Sigma^-]/2$. Now define the octupolar operators as the rank 3 spherical tensor operators, $T_m^{(3)}$ in terms of J_+, J_- and J_z . Note that octupolar operators are time-reversal odd. Thus, under the time-reversal transformation, \mathcal{T} , we have $\mathcal{T}\Sigma^\pm\mathcal{T}^{-1} = -\Sigma_\mp$, $\mathcal{T}\Sigma^z\mathcal{T}^{-1} = -\Sigma^z$. As a result, $\Sigma^z \sim T_0^{(3)}$ and $\Sigma^\pm \sim T_m^{(3)}$ for non-zero m . However, $T_1^{(3)}$ and $T_{-1}^{(3)}$ vanish because $T_{\pm 1}^{(3)}|\pm\rangle$ is not in the doublet eigenspace. Note that $T_{\pm 1}^{(3)}$ changes the eigenvalue of the J_z operator by ± 1 . Similarly, since $J_\pm^2|\pm\rangle$ and $J_\pm^3|\mp\rangle$ are not in the doublet, the only non-trivial matrix elements are $\langle \pm | T_{\pm 2}^{(3)} | \mp \rangle$ and $\langle \mp | T_{\mp 3}^{(3)} | \pm \rangle$. This leads to $T_{\pm 2, \mp 3}^{(3)} \sim \Sigma^\pm$. In detail, one can represent the octupolar pseudospin operators in the doublet as,

$$\Sigma^z \equiv T_0^{(3)}, \quad \Sigma^\pm \equiv \frac{1}{2}\sqrt{\frac{2}{15}}T_{\pm 2}^{(3)} \mp \frac{1}{2}\sqrt{\frac{1}{5}}T_{\mp 3}^{(3)}. \quad (4)$$

Specifically, $T_{\pm 2}^{(3)} = \frac{1}{4}\sqrt{\frac{105}{\pi}}J_\pm^2 J_z$, $T_{\mp 3}^{(3)} = \mp \frac{1}{8}\sqrt{\frac{35}{\pi}}J_\pm^3$, and $T_0^{(3)} = \frac{1}{4}\sqrt{\frac{7}{\pi}}(5J_z^3 - 3J_z J^2)$, where $\bar{\mathcal{O}}$ is the symmetrization of the operator \mathcal{O} ⁷⁴. Each pseudospin operator is a linear combination of rank 3 tensors. From Eq. (4), one can write,

$$\Sigma_{x(y)} = \frac{1}{4}\left[\sqrt{\frac{2}{15}}(T_2^{(3)} \pm T_{-2}^{(3)}) \pm \sqrt{\frac{1}{5}}(T_3^{(3)} - T_{-3}^{(3)})\right], \quad (5)$$

where $x(y)$ takes $+$ ($-$) sign in Eq. (5), respectively. Note that the octupole moment is restricted to the 2-sphere, which represents the set of possible expectation values of the three pseudospin operators, Σ^z and $\Sigma_{x(y)}$.

Generic spin Hamiltonian on symmetry grounds

By applying the symmetry transformation of the icosahedron group (I_h) and the time reversal symmetry transformation, one can find the generic spin Hamiltonian of the nearest neighbor interactions. Let us define the local z -axis pointing to the center of the icosahedron shell. Then, under the 5-fold rotational symmetries of I_h , we have $\Sigma_i^\pm \rightarrow e^{\mp 4i\pi/5} \Sigma_j^\pm$, where i and j are the nearest neighboring sites. This leads to the bond dependent phase factors in the Hamiltonian, such as $\Sigma_i^+ \Sigma_j^+$ or $\Sigma_i^+ \Sigma_j^z$ terms. As a result, the generic symmetry allowed Hamiltonian under the icosahedral symmetry contains four independent parameters, $J_{\pm\pm}$, $J_{\pm z}$, J_\pm and J_{zz} , and is given as,

$$H = \sum_{\langle ij \rangle} \left[J_{zz} \Sigma_i^z \Sigma_j^z + J_\pm \left(\Sigma_i^+ \Sigma_j^- + \Sigma_i^- \Sigma_j^+ \right) + J_{\pm\pm} \left(a_{ij} \Sigma_i^+ \Sigma_j^+ + a_{ij}^* \Sigma_i^- \Sigma_j^- \right) + J_{\pm z} \left(\Sigma_i^z \left(\beta_{ij} \Sigma_j^+ + \beta_{ij}^* \Sigma_j^- \right) + i \leftrightarrow j \right) \right]. \quad (6)$$

Here, a_{ij} takes the values 1 , $e^{\pm i2\pi/5}$ and $e^{\pm i4\pi/5}$ depending on the bond orientation due to the 5-fold rotational symmetry, and $\beta_{ij} = (a_{ij}^*)^2$. The Hamiltonian in Eq. (6) is expressed in terms of local coordinate axes, where the local z -axis for each site is parallel to a high-symmetry axis of the icosahedron (See Supplementary Methods for detailed derivation of the effective pseudospin Hamiltonian and local axes.). The magnitudes of these spin exchange parameters will vary depending on the case. Here, for the simplest case, we first study the Ising limit with a finite J_{zz} and then consider the quantum fluctuations in the presence of J_\pm .

Remarkably, we should emphasize that the spin Hamiltonian, H in Eq. (6), could be used to argue general characteristics of the multipolar pseudospin models even for the C_{5v} symmetry rather than I_h . This is because the constraints on the Hamiltonian have their origin in the mirror reflection symmetry shared by the C_{5v} and I_h groups. See Supplementary Methods and Supplementary Fig. 1 for detailed information. The Hamiltonian in Eq. (6) would be applicable for any Kramers or non-Kramers doublets with half-integer or integer values of J . The only difference between Kramers and non-Kramers doublets is the presence and the absence of the parameter $J_{\pm z}$. This is originated from the fact that for non-Kramers doublet, z components represent magnetic dipoles, whereas x, y components represent quadrupoles or hexadecapoles, thus the coupling between Σ^z and Σ^\pm is forbidden under the time reversal symmetry.

Geometrical frustration

Let us first consider the Ising model, where only J_{zz} is non-zero in Eq. (6). Figure 3 represents the structure of icosahedral quasicrystal descended from 6-dimensional hyperspace by the cut-and-project scheme⁶⁰. As shown in Fig. 3, the distances between the centers of the icosahedrons vary. Particularly, the orthographic projection view of Fig. 3 shows that if we connect two sites of the magnetic atom whose distance is less than or equal to the length of an edge of the icosahedron shell, then there are many isolated icosahedron shells. See Supplementary Methods for detailed cut-and-project scheme for the icosahedral quasicrystal. In real-world materials, the distances between shells may vary depending on the structures of quasicrystals and approximants^{63–66,75}. Furthermore, it is known that the inter-shell distance can be also controlled in terms of the external pressure^{63,76,77}. Thus, for general argument, we mainly focus on the nearest neighboring sites in a single icosahedron and discuss the magnetic states. For ferromagnetic J_{zz} , it is obvious there are

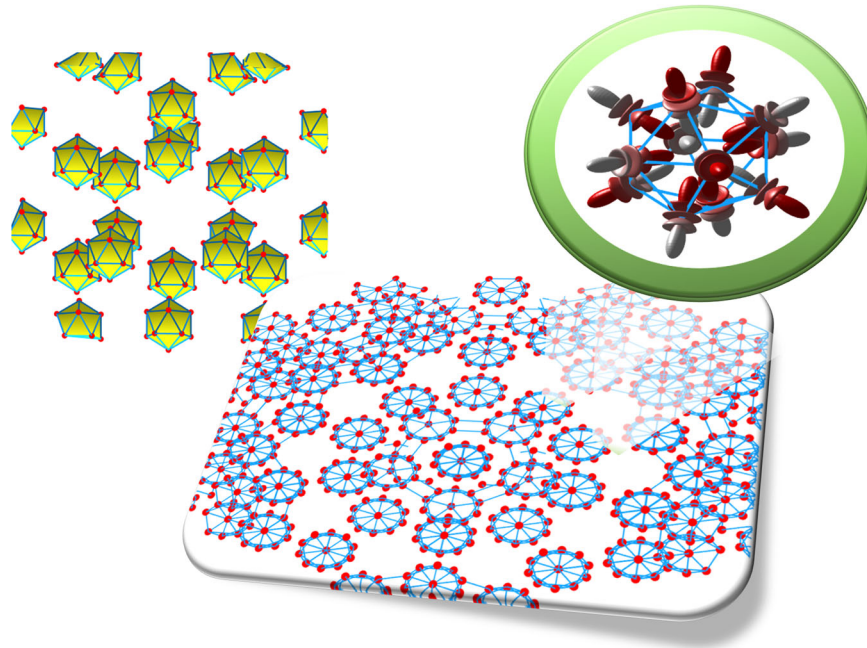


Fig. 3 Icosahedral quasicrystal generated by the cut-and-project scheme from 6-dimensional hyperspace. Red dots represent the sites of the magnetic atom. We draw the sites forming the icosahedron shells only for visibility. The projection view is drawn to emphasize the high-symmetry of the icosahedral quasicrystal. The shortest distance between the centers of the icosahedrons has different values for each icosahedron shell in the quasicrystal. In the projection view, any pair of two sites are connected by the sky-blue line if their distance is less than or equal to the length of an edge of an icosahedron shell. There are many isolated icosahedron shells which have no connection to the other icosahedron shells. For the antiferromagnetic, J_{zz} , there is geometrical frustration on each icosahedron.

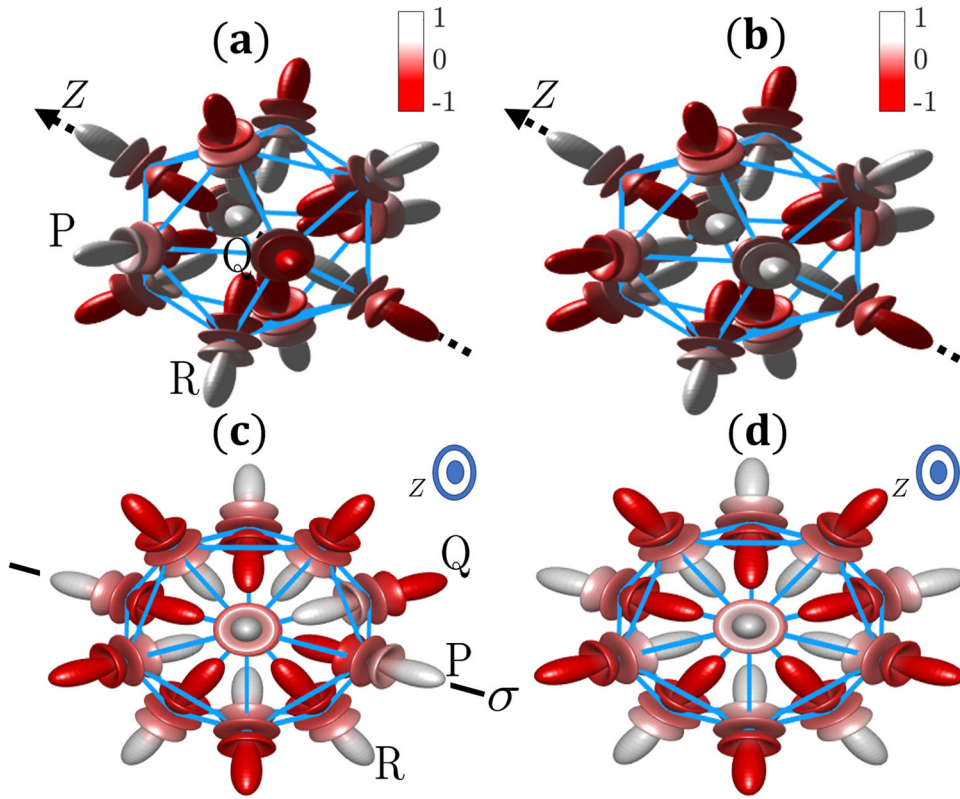


Fig. 4 Two distinct groups of octupolar ground states on an icosahedron for antiferromagnetic J_{zz} based on the symmetry ground. **a** 60 degenerate states with no 5-fold rotational symmetry. **b** 12 degenerate states with 5-fold symmetry. Z -axis is the 5-fold rotational symmetry axis in **(b)**. **c, d** Top view along Z -axis in **(a, b)**, respectively. **(c)** Mirror reflection with respect to σ plane containing Z -axis swaps the octupoles on the sites Q and R . This leads to another degenerate state which lacks the 5-fold symmetry. **d** The state depicted in **(b)** possesses 5-fold rotational symmetry along Z -axis.

only two degenerate ground states, where every octupole points in local $+z$ and $-z$ directions, respectively.

For the antiferromagnetic Ising model, where J_{zz} is positive, the presence of triangular faces in the icosahedron leads to geometric frustration. In this case, there exist 72 degenerate states that are classified into two groups based on symmetry grounds (i) 60 degenerate states without 5-fold rotational symmetry, (ii) 12 degenerate states with 5-fold rotational symmetry. Figure 4a shows an example of the first group of ground states. Note the octupolar moments arranged on the icosahedron in Fig. 4a do not have a 5-fold rotational symmetry axis. Since there are 6 independent choices for the Z -axis, by applying 5-fold rotational transformation around each Z -axis, we have 30 degenerate states. In addition, for each 30 degenerate states, the energy is invariant under the swap of two octupoles on the sites Q and R in Fig. 4a and c. Hence M_σ , the spatial mirror reflection with respect to the σ -plane depicted in Fig. 4c doubles the number of degenerate states with no 5-fold rotational symmetry, resulting in total 60 degenerate states. (See Supplementary Note for detailed discussion of the symmetry argument.). Figure 4b, d illustrate 5-fold rotational symmetric ground state. There are 12 independent choices for the rotational symmetry axis, Z -axis in Fig. 4b of the second group.

Quantum fluctuation

Now let us consider non-zero but small J_\pm and study the effect of quantum fluctuations. To study the fluctuation effects, we introduce three subsets of the 72 degenerate states, A, B and C in terms of the orientation preserving icosahedral rotation group, $I \trianglelefteq I_h$. Specifically, the subsets A and C are generated by applying

the spatial rotations in I to the states in Fig. 4a, b, respectively. While, the subset B is generated by applying the coset, $IM_\sigma = \{gM_\sigma | g \in I\}$ to the state in Fig. 4a. Thus, for $H_\pm = J_\pm \sum_{(i,j)} (\Sigma_i^+ \Sigma_j^- + \Sigma_i^- \Sigma_j^+)$, two states in the same subset admit zero matrix element of H_\pm . One can let $|\psi_{A_n}\rangle$, $|\psi_{B_l}\rangle$ and $|\psi_{C_r}\rangle$, where $1 \leq n, l \leq 30$ and $1 \leq r \leq 12$ be the states in A, B and C, respectively. Hence, in the sub-Hilbert space of the 72 Ising ground states, H_\pm has the matrix representation, $[H_\pm]_{A,B,C}$, given by

$$[H_\pm]_{A,B,C} = \begin{pmatrix} 0 & T_{AB} & T_{AC} \\ T_{BA} & 0 & T_{BC} \\ T_{CA} & T_{CB} & 0 \end{pmatrix} \quad (7)$$

where $T_{BA} = T_{AB}^\dagger$ is a 30×30 matrix, while $T_{AC} = T_{CA}^\dagger$ and $T_{BC} = T_{CB}^\dagger$ are 30×12 matrices. Here, each non-zero matrix element is J_\pm . On symmetry grounds, we can write the general form of the ground state, $|\text{GS}\rangle$, as,

$$|\text{GS}\rangle = a \sum_{n=1}^{30} |\psi_{A_n}\rangle + b \sum_{l=1}^{30} |\psi_{B_l}\rangle + c \sum_{r=1}^{12} |\psi_{C_r}\rangle, \quad (8)$$

where we have only three real coefficients, a, b and c for $|\psi_{A_n}\rangle$, $|\psi_{B_l}\rangle$ and $|\psi_{C_r}\rangle$, respectively (See Supplementary Note for detailed discussion for the perturbative method.). The energy correction is $E(a, b, c) = \langle \text{GS} | H_\pm | \text{GS} \rangle$.

First, considering $J_\pm < 0$, the Lagrange multiplier method leads to $a = b = (1 + \sqrt{6})c/5$ for the ground state. Next, if $J_\pm > 0$, $E(a, b, c)$ is minimized when $a = -b$ and $c = 0$. Remarkably, we have no degeneracy in either cases. Thus, any small quantum

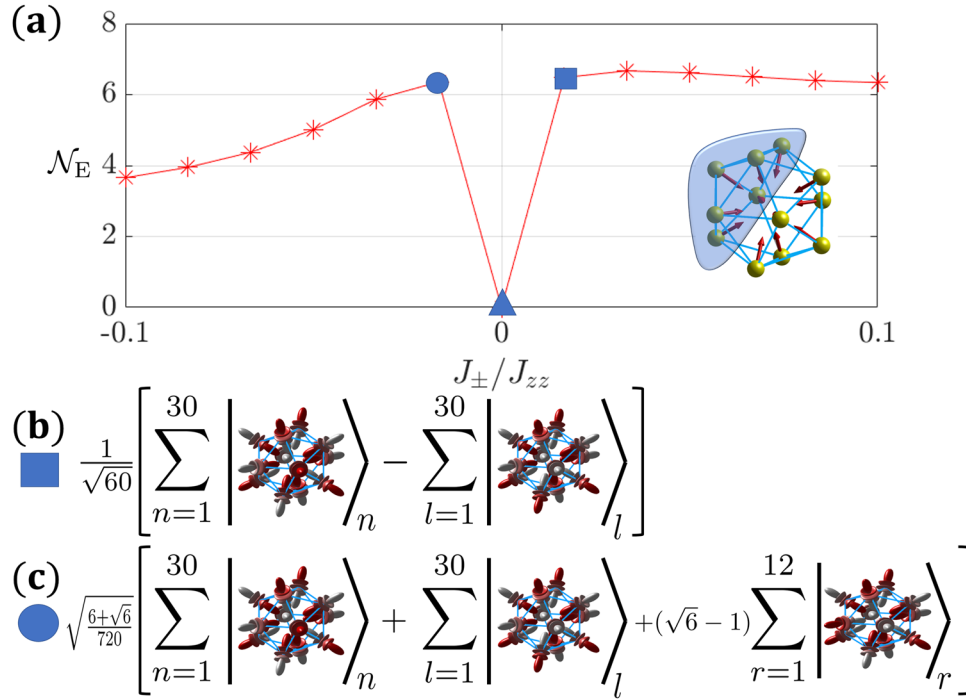


Fig. 5 Quantum fluctuation effect of nonzero J_{\pm} . **a** For nonzero J_{\pm} , the entanglement negativity of the ground state, \mathcal{N}_E , becomes finite. The blue shaded region of the icosahedron, as depicted in the inset, defines the sub-Hilbert space. Red arrows accentuate the local z axes. When $J_{\pm} = 0$ (represented by the triangle), the state is separable. For $J_{\pm} > 0$ (square, **(b)**), the ground state is composed of the states in A and B subsets with equal probability but opposite sign. When $J_{\pm} < 0$ (circle, **(c)**), all 72 degenerate states are combined in the ground state, as shown in **(c)**.

fluctuation given by H_{\pm} leads to a ground state with particular superpositions of degenerate states (See Supplementary Note for detailed derivation).

To capture the entanglement, we compute the entanglement negativity of the state defined by $\mathcal{N}_E = \sum_i (|\lambda_i| - \lambda_i)/2$, where λ_i are all eigenvalues of the partial transpose of the density matrix of the ground state, ρ ⁷⁸. $\mathcal{N}_E = 0$ if ρ is separable, while $\mathcal{N}_E > 0$ for an entangled state. For the icosahedron shell, \mathcal{N}_E is computed by partitioning 12 vertices into two hemispherical region (one of them is highlighted as the blue shaded region in the inset of Fig. 5). Figure 5a illustrates the entanglement is instantaneously generated for non-zero J_{\pm} .

The quantum fluctuation effects originated from $J_{\pm\pm}$ and $J_{\pm z}$ appear in higher-order. In detail, let D and P_D be the subspace of the degenerate ground states of the Ising model (either $J_{zz} < 0$ or $J_{zz} > 0$) and the projection operator to D , respectively. For additional terms in the Hamiltonian, say $H_{\pm\pm} = \sum_{(i,j)} [J_{\pm\pm} \Sigma_i^{\pm} \Sigma_j^{\pm} + h.c.]$ or $H_{\pm z} = \sum_{(i,j)} [J_{\pm z} \Sigma_i^{\pm} \Sigma_j^z + h.c.]$, we have $P_D H_{\pm\pm} P_D = P_D H_{\pm z} P_D = 0$. This is because $J_{\pm\pm}$ and $J_{\pm z}$ terms do not preserve the total Σ^z . Thus, the degeneracy is not lifted at the first-order in perturbation theory. This implies that the quantum fluctuations originated from the J_{++} or J_{+z} terms appear in higher-orders, for instance $P_D H_{++} Q_D H_{\pm\pm} P_D$, where $Q_D = 1 - P_D$. On the other hand, J_{\pm} terms in the Hamiltonian lift the degeneracy at the first-order because $P_D H_{\pm} P_D \neq 0$. As a result, compared to the J_{\pm} term, $J_{\pm\pm}$ and $J_{\pm z}$ select a distinct linear superposition of the degenerate subspace of an icosahedron shell.

Influence of the inter-icosahedron interaction

Now let us discuss the inter-icosahedron interaction effect. See Supplementary Fig. 3 for the case of the ferromagnetic intra-icosahedron Ising interaction. Here, we consider the case of antiferromagnetic intra-icosahedron Ising interaction. Based on the self-similarity of the icosahedral quasicrystal, we have an enlarged

icosahedral structure composed of 12 icosahedron clusters. Taking into account the nearest neighboring sites between the clusters, the interacting sites between the clusters form triangles. These are shown in Fig. 6a, b drawn as orange lines. Since these triangles are not shared, the energy for inter-clusters interaction should be minimized for each triangle. We also note that only 5 sites out of 12 sites in an icosahedron cluster interact with neighboring sites that belong to other icosahedron clusters. Hence, for each icosahedron, there are 7 sites which do not interact with other clusters. The configurations of these 7 sites are only determined by the local intra-cluster interactions. Let us consider the inter-clusters Ising interaction,

$$H_{\text{inter}} = \sum_{(i,j)} J_{\text{inter}} \Sigma_i^z \Sigma_j^z. \quad (9)$$

For both $J_{\text{inter}} > 0$ and $J_{\text{inter}} < 0$, the inter-cluster interactions reduce the whole degeneracy of the enlarged icosahedron structure from 72^{12} , that is composed of 12 icosahedrons. Figure 6a, b show the examples of the ground state configurations of ferromagnetic and antiferromagnetic inter-cluster Ising interaction, respectively. For instance, when $J_{\text{inter}} < 0$, every octupole connected by the orange lines should point either outside or inside of their icosahedron clusters (See the middle and right panels of Fig. 6a). On the other hand, for $J_{\text{inter}} > 0$, additional frustration effect exists on each orange triangle. Figure 6c shows an example of such geometrical frustration due to $J_{\text{inter}} > 0$. In this case, there are more number of frustrated configurations. We emphasize that such geometrical frustration emerges in the enlarged self-similar icosahedral structures in the quasicrystal.

Remarkably, even for the ferromagnetic inter-cluster interaction, the degeneracy of each icosahedron shell is reduced due to the inter-cluster interaction. Once the configuration of a single icosahedron shell is fixed, the configurations of the nearest neighboring icosahedron shells (five of them) are also partially determined due to the ferromagnetic inter-cluster interaction. For

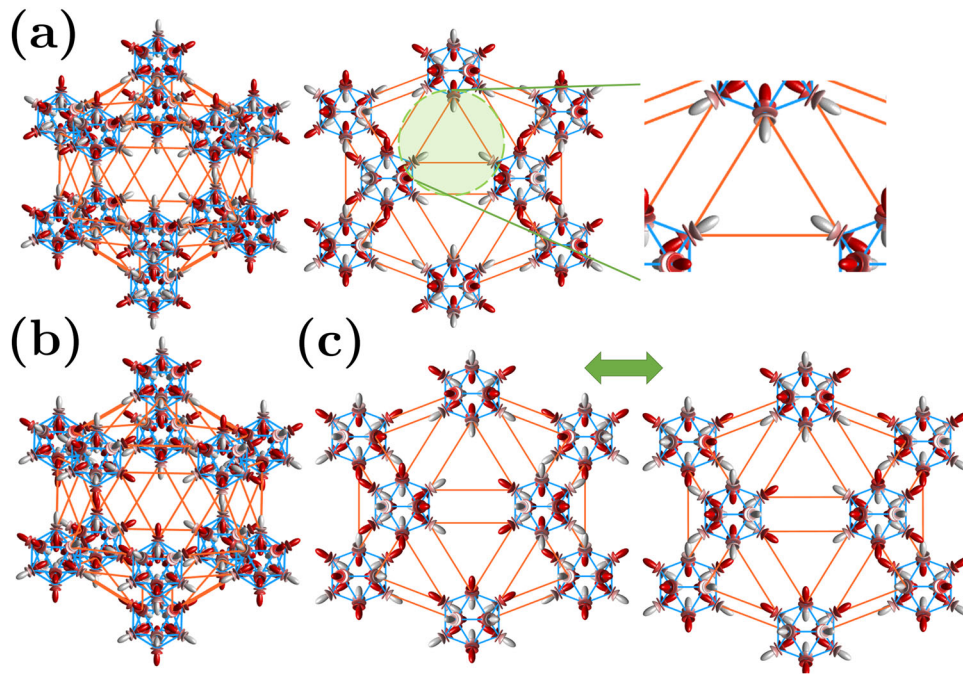


Fig. 6 Examples of the classical octupolar configurations when the intra Ising interaction is antiferromagnetic, $J_{zz} > 0$. **a** $J_{\text{inter}} < 0$ and **(b)** $J_{\text{inter}} > 0$. The orange lines are drawn for emphasizing the inter-cluster interactions. **a** For each orange triangles, three octupoles should point either all-outside or all-inside of their icosahedron. **c** An example of the degenerate ground state due to the frustration of the antiferromagnetic inter-cluster interactions. For $J_{\text{inter}} > 0$, three octupoles for each orange triangles should satisfy 2-in-1-out or 1-in-2-out, which leads to the geometrical frustration on the enlarged spatial scale.

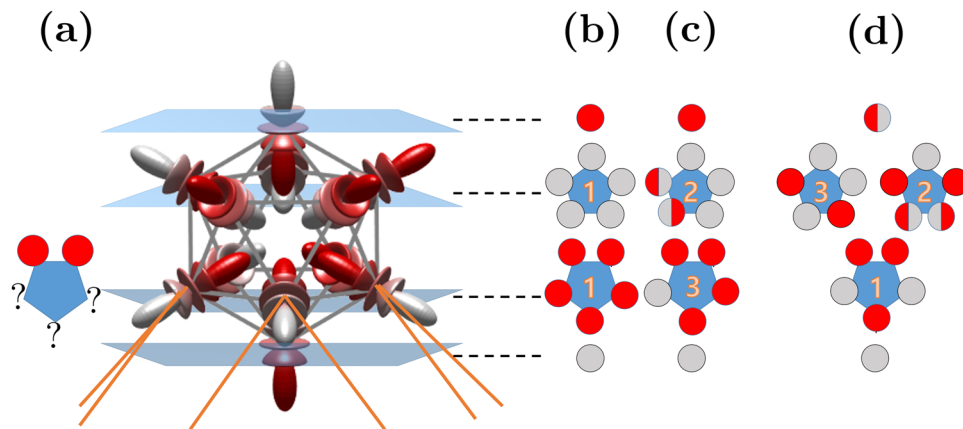


Fig. 7 An example of the frustration on an icosahedron due to the ferromagnetic inter-cluster interactions. **a** For simplicity, we slice an icosahedron into 4 layers, each layer contains 1, 5, 5 and 1 octupoles, respectively. Red (silver) circles represent the octupoles pointing outside (inside) of the icosahedron shell. Half circles emphasize two-fold degrees of freedom. Here, we assume that due to the inter-cluster interactions, two neighboring octupoles are fixed as pointing outside of the icosahedron shell. Then, the octupole located at the bottom in the figure should be pointing inside of the icosahedron. There are three kinds of the configurations on the 5 sites that are interacting with the other icosahedrons. Configuration **(b)** which has all pointing outside configuration belongs to the C group, and hence it determines a configuration in other sites. On the other hand, other two kinds of configurations have further frustrated degrees of freedom. In detail, the configuration **(c)** admits $3 \times 2 = 6$ -fold degeneracy, while the configuration **(d)** admits $3 + 2 = 5$ -fold degeneracy. In total, only 12 fold degeneracy is survived under the inter-cluster interactions.

instance, if the icosahedron shell has the configuration belong to C group whose inter-cluster interacting sites are all pointing out of the icosahedron (red circles in Fig. 7), then at least two inter-cluster interacting octupoles in each neighboring icosahedron also points out of the icosahedron. This reduces the allowed manifold of the antiferromagnetic ground states on the neighboring icosahedron clusters. Refer to Fig. 7 for a specific example of this reduction.

One may ask the influence of the quantum fluctuation under the inter-icosahedron interaction. To address it, we consider $|J_{\text{inter}}| > \Delta$ where Δ is the gap of the first excited state of an isolated icosahedron shell with intra-shell J_{\pm} . See Supplementary Fig. 4 for detailed information of the gap. First of all, for both cases of the sign of J_{inter} , it selects particularly degenerate manifold among 72 states. This is because the inter-shell interaction (partially) selects the configurations of the sites in neighboring icosahedrons. For

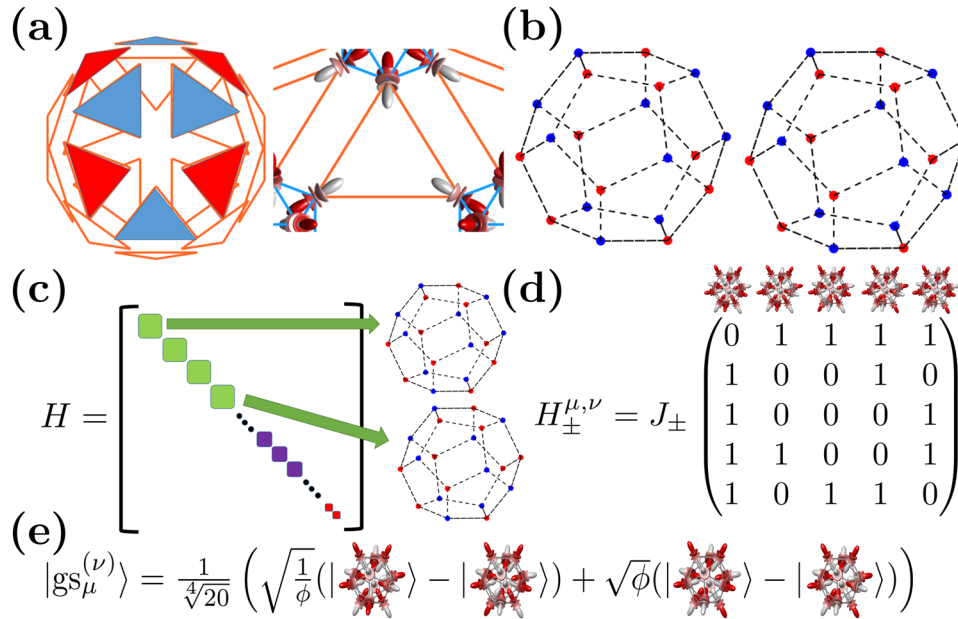


Fig. 8 Selection of the ground state in the presence of both J_{inter} and intra-shell quantum fluctuation. **a** Geometrical structure of the inter-shell interactions (orange lines). For $J_{\text{inter}} < 0$, ferromagnetic Ising inter-shell interactions, each separated triangles of orange lines should admit either all-in- or all-out octupole configurations as exemplified in the right panel. In the left panel, we assign red and blue colors on some triangles as the all-in-, and all-out-pointing configurations, respectively. **b** 60 inter-shell interacting sites and their interactions mapped onto a dodecahedron, which is a dual of the icosahedron. Here, red and blue dots correspond to the red and blue triangles including three octupoles in (a). Dashed black lines connect two dots if these two dots (originally red or blue triangles) contain the sites belonging to original single icosahedron shell. **c** Block diagonalized Hamiltonian including intra-shell J_{zz} , J_{\pm} and inter-shell Ising interaction, J_{inter} . The blocks of the Hamiltonian are classified in terms of the configurations of the 60 inter-shell i.e. the configurations on the dodecahedrons in (b). The maximal dimension of the sub-Hilbert space is 5^{12} which is much smaller than the total dimension, 72^{12} (the case for $J_{\text{inter}} = 0$). **d** Effective Hamiltonian for the quantum fluctuation on μ -th icosahedron for ν -th 5^{12} -dimensional sub-Hilbert space, written as $H_{\pm}^{\mu,\nu}$. The basis are chosen as the 5-types of configurations on a shell (See Fig. 6(c)). **e** The ground state of $H_{\pm}^{\mu,\nu}$ for $J_{\pm} > 0$ for μ -th icosahedron, $|gs_{\mu}^{(\nu)}\rangle$. Here, $\phi = (1 + \sqrt{5})/2$ is the golden ratio. The ground state defined in the enlarged icosahedral structure is classified by the configurations of 60 inter-shell interacting octupoles as $|GS^{(\nu)}\rangle = \otimes_{\mu=1}^{12} |gs_{\mu}^{(\nu)}\rangle$.

instance, for $J_{\text{inter}} < 0$, each separated orange triangles in the right panel of Fig. 6a should admit either all-in- or all-out octupole configurations. This reduces the ground state manifold of the enlarged icosahedral structure from 72^{12} dimensions, which is realized in the absence of inter-shell interaction. Note that without quantum fluctuations on each icosahedron shell, the allowed ground states could be written as the product state i.e. $|GS\rangle = \otimes_{i=1}^{12} |\psi_{k_i}^{(i)}\rangle$. Here, $1 \leq k_i \leq 72$ is the index of 72 kinds of allowed antiferromagnetic frustrated ground configurations on an isolated icosahedron shell. However, importantly, only certain set of k_i is selected if we take into account J_{inter} .

To address quantum fluctuations, let us consider the intra-shell, J_{\pm} term. We neglect the inter-shell interaction J_{\pm} , because it would be much smaller than both inter-shell Ising interactions and intra-shell quantum fluctuations. Since intra-shell J_{\pm} term only flips two neighboring octupoles in the same icosahedron shell, two ground states, say $|GS_a\rangle$ and $|GS_b\rangle$ such that $\langle GS_a | H_{\pm} | GS_b \rangle \neq 0$ have to be obtained by flipping two neighboring octupoles in an icosahedron shell, keeping all other octupoles unchanged. However, for $J_{\text{inter}} < 0$, if we flip an octupole on an icosahedron shell that is interacting with neighboring icosahedron shells, then the octupoles in different icosahedron shells also should be flipped due to the inter-shell interaction. Thus, $|GS_a\rangle$ and $|GS_b\rangle$ should share the same configuration of the 60 inter-shell interacting sites. Hence, one can classify the state that are mixed due to J_{\pm} in terms of the configurations of the 60 inter-shell interacting sites.

Figure 8 explains how the ground states are chosen in the presence of both the inter-shell interactions and intra-shell

quantum fluctuations. Although we assume $J_{\text{inter}} < 0$, here, the similar argument would be applicable for $J_{\text{inter}} > 0$ along with additional frustration effects on the orange triangle. Note that J_{inter} restricts the possible octupole configurations on each separated triangles as shown in Fig. 8a. Here, blue and red triangles represent all-in-, and all-out-pointing octupoles configurations, as exemplified in the right panel of Fig. 8a. Thus, the classical ground states are classified in terms of the configurations of these 20 triangles, red or blue colored. Based on the duality of the icosahedron, the configurations of 20 triangles are mapped onto the sites in the dodecahedrons as shown in Fig. 8b. In detail, the red and blue dots in Fig. 8b correspond to the red and blue triangles in Fig. 8a. The dashed lines are drawn if there are the sites connected by the intra-shell interactions in neighboring triangles. The Hilbert space is factorized into many sub-Hilbert spaces classified in terms of the configurations of the dodecahedron i.e. inter-shell interacting 60 sites, and hence the Hamiltonian, H is now block diagonalized as shown in Fig. 8c. The ground state is originated from the largest dimensional sub-Hilbert space. In Fig. 7a–c, we see that the maximal dimension of a sub-Hilbert space is 5^{20} when all the icosahedron shells correspond to the case of Fig. 7c. Indeed, Fig. 8b shows two examples of the dodecahedrons correspond to the 5^{20} -dimensional sub-Hilbert spaces. Figure 8c represents these maximal dimensional sub-Hilbert space as the green squares. Furthermore, since the quantum fluctuation is intra-shell interaction, the ground state of the sub-Hilbert space is given by the product state of the ground state of each icosahedron shell. The intra-shell J_{\pm} Hamiltonian on an icosahedron shell is given by 5×5 matrix

which is much smaller than the case of the isolated icosahedron shell, 72×72 matrix. Explicit forms of the H_{\pm} matrix and the ground state (assuming $J_{\pm} > 0$) is shown in Fig. 8d, e, respectively. Here, ν and μ are the indices of the sub-Hilbert space and icosahedron shells, respectively. $\phi = (1 + \sqrt{5})/2$ is the golden ratio. As a result, we have a ground state given $|\text{GS}^{(\nu)}\rangle = \otimes_{\mu=1}^{\mu=12} |g_{\mu}^{(\nu)}\rangle$ for each ν -th sub-Hilbert spaces. Thus, we have large degeneracy of the ground states. Note that such degeneracy would be lifted by the inter-shell J_{\pm} that is small compared to other parameters in general. We emphasize that the inter-shell interactions reduce the ground state manifold, and hence the ground state on each icosahedron shell is changed.

Lastly, let us briefly explain the potential influence of the further neighbor interactions. First, further inter-cluster interactions between neighbors affect the sites that do not interact with neighboring icosahedrons. This further reduces the degeneracy. Second, isolated icosahedron clusters also begin to interact via further neighbor interactions and should be considered. Nevertheless, we suspect that our discussion of the nearest neighbor inter-cluster interaction can be applied analogously to investigate the configurations of the more extended icosahedral structures based on the repetitive self-similar structure of the quasicrystal.

DISCUSSION

In summary, our findings indicate that magnetic quasicrystalline systems contain multipolar degrees of freedom, which arise from the interplay between spin-orbit coupling and CEF splitting of the icosahedral point group symmetry. Despite extensive prior research on magnetic properties in quasicrystals, the presence and significance of multipolar degrees of freedom have yet to be identified. In our study, we demonstrate for the first time that noncrystallographic point group symmetry can accommodate unconventional degrees of freedom and we examine their characteristics. The multipole degrees of freedom are clarified for different values of J , depending on whether there is perfect icosahedral symmetry I_h or five-fold symmetry C_{5v} . Strikingly, it has been demonstrated that pure octupolar degrees of freedom emerge for $J = 7/2$ under I_h symmetry. In this case, the Kramers doublet has zero expectation values for both magnetic dipoles and quadrupoles, but the rank 3 tensors describing the octupole degrees of freedom have nonzero expectation values. Based on the symmetry transformation, we further clarify each component of the pseudospin-1/2 in terms of magnetic octupoles as discussed in Eq. (4). On symmetry grounds, we also derive the spin Hamiltonian with four independent parameters. For anti-ferromagnetic Ising model, magnetic frustration leads to 72 degenerate states for a single icosahedron. For a small but finite J_{\pm} , quantum fluctuations make a particular mixture of these degenerate states. It makes different but non-degenerate ground state for (anti-) ferromagnetic J_{\pm} , producing a finite entanglement even for arbitrary small J_{\pm} . In addition, we show that the inter-icosahedron interaction prefers a particularly degenerate manifold among the 72 states in each icosahedron shell, and thus selects a different mixture of the Ising states under the intra-shell interaction J_{\pm} . Depending on the inter-shell distances, possible macroscopic degeneracy and entanglement of octupoles would be an interesting future work. The self-similarity of the quasicrystals would allow the real-space renormalization group approach to explore potential quantum phase transitions. Note that such self-similar structures are absent in the periodic approximants. Also, the studies in the presence of $J_{\pm\pm}$ and $J_{\pm z}$, which do not preserve the total S^z , can be explored which we leave as a future work.

Such octupolar degrees of freedom can be found in rare-earth based magnetic quasicrystals and approximants such as Au-Al alloys, Cd-Mg alloys including rare earth ions and etc.^{6,49,62–64,68,71,79–85}. However, many of the currently known

magnetic quasicrystals have problems with intermediate valences and some mixed sites between non-rare earth atoms^{79,80,82,85–92}. It makes imperfect symmetries, allowing small deviations from perfect non-crystallographic point group symmetries. Nevertheless, it is expected that advances in chemical synthesis techniques could make the successful synthesis of finely controlled icosahedral quasicrystals possible^{80,83,87,93}, and it may give us a chance to discover pure magnetic octupoles or even higher order multipolar degrees of freedom and their intriguing physics.

To detect the pure octupolar orders, one can use the symmetry allowed higher order time-reversal odd fields. For instance, one can detect the z component of the octupoles by coupling to the magnetic field tensor which has the same symmetry as $5B_z^3 - 3B_z(\mathbf{B} \cdot \mathbf{B})$, where \mathbf{B} is the external magnetic field and B_z is its z component. Also, one can use the magnetostriction effect as discussed in refs. ^{59,94,95}.

Our work shows that the multipolar degrees of freedom arise naturally in icosahedral quasicrystals. It breaks the ground in the magnetism of quasicrystals and raises several interesting questions. One could explore magnetic quasicrystals looking for hidden phases, magnetic frustration induced long-range entanglement such as spin liquids and non-Fermi liquids due to the exotic Kondo effect^{6,96–99,99–101}. Our study motivates to experimentally find rare-earth icosahedral quasicrystals beyond conventional magnetism in periodic crystals. The field of magnetic quasicrystals is an interesting research area, and continuous progress in both experimental and theoretical studies is leading us to discover anomalous magnetic phenomena in quasicrystals.

METHODS

Exploration of the multipoles

To construct the crystal electric field (CEF) Hamiltonian, we utilized the simplified point charge model. In this model, point charge ligands are positioned on each of the 12 vertices of the icosahedron that surrounds the rare earth atom. For the charge impurity model, where the icosahedral point group symmetry breaks down to the C_{5v} , we place the charge impurity at the ligand site on the local z -axis. The Stevens parameter is calculated using numerical values of the Stevens factors and radial integrals of rare-earth ions, as presented in¹⁰². Our method involves block diagonalizing the CEF Hamiltonians and searching for possible doublet eigenspaces and their corresponding multipolar degrees of freedom. We determine the presence of higher-order multipolar degrees of freedom by examining the vanishing of lower magnetic or electric multipole operators. To construct the spin Hamiltonian that is allowed by symmetry on the icosahedral quasicrystal, we apply both the icosahedral point group symmetry and time-reversal symmetry to the octupolar pseudospin operators. Further details are described in the Supplementary Methods.

Construction of the icosahedral quasicrystal

The icosahedral quasicrystal is constructed using the standard cut-and-project scheme explained in detail in the Supplementary Methods. To find the ground states of the Ising model under open boundary conditions, we utilized the exact diagonalization method and symmetry ground. Using quantum fluctuation, we have conducted an analytical study on the entangled pure ground state and computed its entanglement negativity on the single icosahedron shell through the exact diagonalization method.

DATA AVAILABILITY

The data that support the findings of this study are available from the corresponding author upon request.

CODE AVAILABILITY

The code that support the findings of this study are available from the authors upon request.

Received: 20 September 2023; Accepted: 22 December 2023;
Published online: 06 January 2024

REFERENCES

- Buyers, W. J. L. Low moments in heavy-fermion systems. *Phys. B Condens. Matter* **223**, 9–14 (1996).
- Shah, N., Chandra, P., Coleman, P. & Mydosh, J. Hidden order in URu₂Si₂. *Phys. Rev. B* **61**, 564 (2000).
- Chakravarty, S., Laughlin, R., Morr, D. K. & Nayak, C. Hidden order in the cuprates. *Phys. Rev. B* **63**, 094503 (2001).
- Mydosh, J. A. & Oppeneer, P. M. Colloquium hidden order, superconductivity, and magnetism the unsolved case of URu₂Si₂. *RMP* **83**, 1301 (2011).
- Mydosh, J. A. & Oppeneer, P. M. Hidden order behaviour in URu₂Si₂ (a critical review of the status of hidden order in 2014). *Philos. Magn.* **94**, 3642–3662 (2014).
- Tamura, R. et al. Experimental observation of long-range magnetic order in icosahedral quasicrystals. *J. Am. Chem. Soc.* **143**, 19938–19944 (2021).
- Vasiliev, A., Volkova, O., Zvereva, E. & Markina, M. Milestones of low-D quantum magnetism. *Npj Quant. Mater.* **3**, 18 (2018).
- Erkelens, W. A. C. et al. Neutron scattering study of the antiferroquadrupolar ordering in CeB₆ and Ce_{0.75}La_{0.25}B₆. *J. Magn. Magn. Mater.* **63–64**, 61–63 (1987).
- Kitagawa, J., Takeda, N. & Ishikawa, M. Possible quadrupolar ordering in a Kondo-lattice compound Ce₃Pd₂₀Ge₆. *Phys. Rev. B* **53**, 5101 (1996).
- Shiina, R., Shiba, H. & Thalmeier, P. Magnetic-field effects on quadrupolar ordering in a γ 8-quartet system CeB₆. *J. Phys. Soc. Jpn.* **66**, 1741–1755 (1997).
- Lingg, N., Maurer, D., Müller, V. & McEwen, K. Ultrasound investigations of orbital quadrupolar ordering in UPd₃. *Phys. Rev. B* **60**, 8430 (1999).
- Yamauchi, H. et al. Antiferroquadrupolar ordering and magnetic properties of the tetragonal DyB₂C₂ compound. *J. Phys. Soc. Jpn.* **68**, 2057–2066 (1999).
- Tanaka, Y. et al. Evidence of antiferroquadrupolar ordering of DyB₂C₂. *J. Phys. Condens.* **11**, 505 (1999).
- Kitagawa, J. et al. Third-order magnetic susceptibility and quadrupolar order parameter of Kondo-Lattice compound Ce₃Pd₂₀Ge₆. *J. Phys. Soc. Jpn.* **69**, 883–887 (2000).
- Tayama, T. et al. Antiferro-quadrupolar ordering and multipole interactions in PrPb₃. *J. Phys. Soc. Jpn.* **70**, 248–258 (2001).
- Iwasa, K. et al. Crystal-structure modulation in the anomalous low-temperature phase of PrFe₄P₁₂. *Phys. B Condens. Mater.* **312**, 834–836 (2002).
- Matsuoka, E., Kitagawa, J., Ohyama, K., Yoshizawa, H. & Ishikawa, M. Evidence of the quadrupolar ordering in DyPd₃S₄. *J. Phys. Condens.* **13**, 11009 (2001).
- Buschow, K. J. *Handbook of Magnetic Materials* 5th edn, Vol. 15 (Elsevier Amsterdam, 2003).
- Hotta, T. Multipole fluctuations in filled skutterudites. *J. Phys. Soc. Jpn.* **74**, 2425–2429 (2005).
- Kiss, A. & Fazekas, P. Group theory and octupolar order in URu₂Si₂. *Phys. Rev. B* **71**, 054415 (2005).
- Yanagisawa, T. et al. Dilatometric measurements and multipole ordering in DyB₂C₂ and HoB₂C₂. *J. Phys. Soc. Jpn.* **74**, 1666–1669 (2005).
- Kiss, A. & Kuramoto, Y. Scalar order possible candidate for order parameters in skutterudites. *J. Phys. Soc. Jpn.* **75**, 103704 (2006).
- Santini, P., Carretta, S., Magnani, N., Amoretti, G. & Caciuffo, R. Hidden order and low-energy excitations in NpO₂. *Phys. Rev. Lett.* **97**, 207203 (2006).
- Tanida, H., S. Suzuki, H., Takagi, S., Onodera, H. & Tanigaki, K. Possible low-temperature strongly correlated electron behavior from multipole fluctuations in PrMg₃ with cubic non-Kramers γ 3 doublet ground state. *J. Phys. Soc. Jpn.* **75**, 073705 (2006).
- Matsuoka, E. et al. Simultaneous occurrence of an antiferroquadrupolar and a ferromagnetic transitions in rare-earth palladium bronze CePd₃S₄. *J. Phys. Soc. Jpn.* **77**, 114706–114706 (2008).
- Carretta, S., Santini, P., Caciuffo, R. & Amoretti, G. Quadrupolar waves in uranium dioxide. *Phys. Rev. Lett.* **105**, 167201 (2010).
- Cricchio, F., Bultmark, F., Grånäs, O. & Nordström, L. Itinerant magnetic multipole moments of rank five as the hidden order in URu₂Si₂. *Phys. Rev. Lett.* **103**, 107202 (2009).
- Kusunose, H. & Harima, H. On the hidden order in URu₂Si₂—antiferro hexadecapole order and its consequences. *J. Phys. Soc. Jpn.* **80**, 084702 (2011).
- Ano, G. et al. Quadrupole ordering and rattling motion of clathrate compound Pr₃Pd₂₀Ge₆. *J. Phys. Soc. Jpn.* **81**, 034710 (2012).
- Onimaru, T. et al. Antiferroquadrupolar ordering in a Pr-based superconductor PrIr₂Zn₂₀. *Phys. Rev. Lett.* **106**, 177001 (2011).
- Goho, T. & Harima, H. Electronic structure with antiferro-electric-multipole ordering in PrRu₄P₁₂. *J. Phys. Conf.* **592**, e012100 (2015).
- Onimaru, T. & Kusunose, H. Exotic quadrupolar phenomena in Non-Kramers doublet systems—the cases of Pr T₂Zn₂₀ (T = Ir, Rh) and PrT₂Al₂₀ (T = V, Ti)–. *J. Phys. Soc. Jpn.* **85**, 082002 (2016).
- Suzuki, M.-T., Ikeda, H. & Oppeneer, P. M. First-principles theory of magnetic multipoles in condensed matter systems. *J. Phys. Soc. Jpn.* **87**, 041008 (2018).
- Cox, D. Quadrupolar kondo effect in uranium heavy-electron materials? *Phys. Rev. Lett.* **59**, 1240 (1987).
- Tselvik, A. & Reizer, M. Phenomenological theory of non-fermi-liquid heavy-fermion alloys. *Phys. Rev. B* **48**, 9887 (1993).
- Tou, H. et al. Sb-NQR probe for multipole degree of freedom in the first Pr-based heavy-fermion superconductor PrOs₄Sb₁₂. *J. Phys. Soc. Jpn.* **74**, 2695–2698 (2005).
- Walker, M. et al. Nature of the order parameter in the heavy-fermion system URu₂Si₂. *Phys. Rev. Lett.* **71**, 2630 (1993).
- Bauer, E., Frederick, N., Ho, P.-C., Zapf, V. & Maple, M. Superconductivity and heavy fermion behavior in PrOs₄Sb₁₂. *Phys. Rev. B* **65**, 100506 (2002).
- Kohji, M. et al. Evidence for magnetic-field-induced quadrupolar ordering in the heavy-fermion superconductor PrOs₄Sb₁₂. *J. Phys. Soc. Jpn.* **72**, 1002–1005 (2003).
- Suzuki, O. et al. Quadrupolar kondo effect in non-Kramers doublet system PrInAg₂. *J. Phys. Soc. Jpn.* **75**, 013704 (2005).
- Kotegawa, H. et al. Anomalous Kondo effect and ordered state in heavy fermion system SmOs₄Sb₁₂ resistivity, Sb-NQR, and magnetization measurements under high pressure. *J. Phys. Soc. Jpn.* **77**, 90–95 (2008).
- Sakai, A. & Nakatsuji, S. Kondo effects and multipolar order in the cubic PrTr₂Al₂₀ (Tr = Ti, V). *J. Phys. Soc. Jpn.* **80**, 063701 (2011).
- Tsujimoto, M., Matsumoto, Y., Tomita, T., Sakai, A. & Nakatsuji, S. Heavy-fermion superconductivity in the quadrupole ordered state of PrV₂Al₂₀. *Phys. Rev. Lett.* **113**, 267001 (2014).
- Sumita, S. & Yanase, Y. Superconductivity in magnetic multipole states. *Phys. Rev. B* **93**, 224507 (2016).
- Onimaru, T. et al. Quadrupole-driven non-fermi-liquid and magnetic-field-induced heavy fermion states in a non-Kramers doublet system. *Phys. Rev. B* **94**, 075134 (2016).
- Gao, B. et al. Experimental signatures of a three-dimensional quantum spin liquid in effective spin-1/2 Ce₂Zr₂O₇ pyrochlore. *Nat. Phys.* **15**, 1052–1057 (2019).
- Gaudet, J. et al. Quantum spin ice dynamics in the dipole-octupole pyrochlore magnet Ce₂Zr₂O₇. *Phys. Rev. Lett.* **122**, 187201 (2019).
- Sibille, R. et al. A quantum liquid of magnetic octupoles on the pyrochlore lattice. *Nat. Phys.* **16**, 546–552 (2020).
- Sato, T. J. et al. Antiferromagnetic spin correlations in the Zn-Mg-Ho icosahedral quasicrystal. *Phys. Rev. B* **61**, 476–486 (2000).
- Totsuka, K. & Suzuki, M. Matrix formalism for the VBS-type models and hidden order. *Phys. Condens.* **7**, 1639 (1995).
- Aoki, Y., Sugawara, H., Hisatomo, H. & Sato, H. Novel kondo behaviors realized in the filled skutterudite structure. *J. Phys. Soc. Jpn.* **74**, 209–221 (2005).
- Santini, P. et al. Multipolar interactions in f-electron systems The paradigm of actinide dioxides. *RMP* **81**, 807 (2009).
- Tazai, R. & Kontani, H. Multipole fluctuation theory for heavy fermion systems application to multipole orders in CeB₆. *Phys. Rev. B* **100**, 241103 (2019).
- Mydosh, J., Oppeneer, P. M. & Riseborough, P. Hidden order and beyond an experimental-theoretical overview of the multifaceted behavior of URu₂Si₂. *J. Phys. Condens.* **32**, 143002 (2020).
- Patri, A. S., Hosoi, M., Lee, S. & Kim, Y. B. Theory of magnetostriction for multipolar quantum spin ice in pyrochlore materials. *Phys. Rev. Res.* **2**, 033015 (2020).
- Park, P. et al. Field-tunable toroidal moment and anomalous hall effect in noncollinear antiferromagnetic weyl semimetal Co_{1/3}TaS₂. *Npj Quant. Mater.* **7**, 42 (2022).
- Cohen, M.L. & Louie, S.G. *Fundamentals of Condensed Matter Physics* (Cambridge University Press, 2016).
- Mustonen, O. et al. Valence bond glass state in the 4 d¹ fcc antiferromagnet Ba₂LuMoO₆. *Npj Quant. Mater.* **7**, 74 (2022).
- Voleti, S., Pradhan, K., Bhattacharjee, S., Saha-Dasgupta, T. & Paramakanti, A. Probing octupolar hidden order via janus impurities. *Npj Quant. Mater.* **8**, 42 (2023).
- Kellendonk, J., Lenz, D., Savinien, J. *Mathematics of Aperiodic Order* 8th edn, Vol. 309 (Springer London, 2015)
- Suck, J.B., Schreiber, M., Haussler, P. *Quasicrystals An Introduction to Structure, Physical Properties and Applications* 2nd edn, Vol. 55. (Springer London, 2013).
- Labib, F. et al. Magnetic properties of icosahedral quasicrystals and their cubic approximants in the Cd–Mg–RE (RE = Gd, Tb, Dy, Ho, Er, and Tm) systems. *J. Phys. Condens.* **32**, 415801 (2020).

63. Deguchi, K. et al. Quantum critical state in a magnetic quasicrystal. *Nat. Mater.* **11**, 1013–1016 (2012).
64. Suzuki, S. et al. Magnetism of Tsai-type quasicrystal approximants. *Mater. Trans.* **62**, 298–306 (2021).
65. Takeuchi, R. et al. High phase-purity and composition-tunable ferromagnetic icosahedral quasicrystal. *Phys. Rev. Lett.* **130**, 176701 (2023).
66. De Boissieu, M. et al. Lattice dynamics of the Zn–Mg–Sc icosahedral quasicrystal and its Zn–Sc periodic 1/1 approximant. *Nat. Mater.* **6**, 977–984 (2007).
67. Judd, B. R.-N. A crystal field of icosahedral symmetry. *Proc. R. Soc. A Math. Phys. Eng. Sci.* **241**, 122–131 (1957).
68. Kashimoto, S., Matsuo, S., Nakano, H., Shimizu, T. & Ishimasa, T. Magnetic and electrical properties of a stable Zn–Mg–Ho icosahedral quasicrystal. *Solid State Commun.* **109**, 63–67 (1998).
69. Scheie, A. *PyCrystalField* software for calculation, analysis and fitting of crystal electric field Hamiltonians. *J. Appl. Crystallogr.* **54**, 356–362 (2021).
70. Hutchings, M.T. Point-charge calculations of energy levels of magnetic ions in crystalline electric fields. In *Solid State Physics 227–273* (Academic Press, 1964).
71. Walter, U. Crystal-field splitting in icosahedral symmetry. *Phys. Rev. B* **36**, 2504 (1987).
72. Lindgard, P.-A. Tables of products of tensor operators and Stevens operators. *J. Phys. C Solid State Phys.* **8**, 3401 (1975).
73. Sandberg, L. Ø. et al. Emergent magnetic behavior in the frustrated $\text{Yb}_3\text{Ga}_5\text{O}_{12}$ garnet. *Phys. Rev. B* **104**, 064425 (2021).
74. Sakurai, J.J. & Commins, E.D. *Modern Quantum Mechanics Revised edn* (American Association of Physics Teachers, 1995).
75. Steinhart, P.J. & Ostlund, S. *The Physics of Quasicrystals* (World Scientific Singapore, 1987).
76. Berns, V. M. & Fredrickson, D. C. Problem solving with pentagons Tsai-type quasicrystal as a structural response to chemical pressure. *Inorg. Chem.* **52**, 12875–12877 (2013).
77. Watanuki, T. et al. Pressure-induced phase transitions in the Cd–Yb periodic approximant to a quasicrystal. *Phys. Rev. Lett.* **96**, 105702 (2006).
78. Horodecki, R., Horodecki, P., Horodecki, M. & Horodecki, K. Quantum entanglement. *RMP* **81**, 865 (2009).
79. Watanabe, S. Topological magnetic textures and long-range orders in terbium-based quasicrystal and approximant. *PNAS* **118**, 2112202118 (2021).
80. Watanuki, T., Kawana, D., Machida, A. & Tsai, A. Pressure-induced formation of intermediate-valence quasicrystalline system in a Cd–Mg–Yb alloy. *Phys. Rev. B* **84**, 054207 (2011).
81. Sato, T. J., Guo, J. & Tsai, A. P. Magnetic properties of the icosahedral Cd–Mg–rare-earth quasicrystals. *J. Phys. Condens.* **13**, 105 (2001).
82. Imura, K. et al. Variation of pressure-induced valence transition with approximation degree in Yb-based quasicrystalline approximants. *J. Phys. Soc. Jpn.* **92**, 093701 (2023).
83. Yamada, T. et al. Formation of an intermediate valence icosahedral quasicrystal in the Au–Sn–Yb system. *Inorg. Chem.* **58**, 9181–9186 (2019).
84. Sato, T. J. et al. Whirling spin order in the quasicrystal approximant $\text{Au}_{72}\text{Al}_{14}\text{Tb}_{14}$. *Phys. Rev. B* **100**, 054417 (2019).
85. Hiroto, T., Tokiwa, K. & Tamura, R. Sign of canted ferromagnetism in the quasicrystal approximants Au–SM–R (SM = Si, Ge and Sn/R = Tb, Dy and Ho). *J. Phys. Condens.* **26**, 216004 (2014).
86. Watanuki, T. et al. Intermediate-valence icosahedral Au–Al–Yb quasicrystal. *Phys. Rev. B* **86**, 094201 (2012).
87. Lehr, G. J., Morelli, D. T., Jin, H. & Heremans, J. P. Enhanced thermoelectric power factor in $\text{Yb}_{1-x}\text{Sc}_x\text{Al}_2$ alloys using chemical pressure tuning of the Yb valence. *J. Appl. Phys.* **114**, 223712 (2013).
88. Matsukawa, S. et al. Valence change driven by constituent element substitution in the mixed-valence quasicrystal and approximant Au–Al–Yb. *J. Phys. Soc. Jpn.* **83**, 034705 (2014).
89. Otsuki, J. & Kusunose, H. Distributed hybridization model for quantum critical behavior in magnetic quasicrystals. *J. Phys. Soc. Jpn.* **85**, 073712 (2016).
90. Watanabe, S. & Miyake, K. Origin of quantum criticality in Yb–Al–Au approximant crystal and quasicrystal. *J. Phys. Soc. Jpn.* **85**, 063703 (2016).
91. Hayashi, M., Deguchi, K., Matsukawa, S., Imura, K. & Sato, N. K. Observation of systematic variation in Yb ion valence as a function of interatomic spacing in icosahedral approximant crystals. *J. Phys. Soc. Jpn.* **86**, 043702 (2017).
92. Watanabe, S. Magnetism and topology in Tb-based icosahedral quasicrystal. *Sci. Rep.* **11**, 17679 (2021).
93. Nagaoka, Y., Schneider, J., Zhu, H. & Chen, O. Quasicrystalline materials from non-atom building blocks. *Matter* **6**, 30–58 (2023).
94. Sorensen, M. E. & Fisher, I. R. Proposal for methods to measure the octupole susceptibility in certain cubic pr compounds. *Phys. Rev. B* **103**, 155106 (2021).
95. You, Y. et al. Cluster magnetic octupole induced out-of-plane spin polarization in antiperovskite antiferromagnet. *Nat. Commun.* **12**, 6524 (2021).
96. Kimura, K., Hashimoto, T. & Takeuchi, S. Temperature and magnetic field dependence of electrical resistivity in Al–Mn quasicrystal at low temperatures. *J. Phys. Soc. Jpn.* **55**, 1810–1813 (1986).
97. WIDOM, M. Short-and long-range icosahedral order in crystals, glass, and quasicrystals. In *Aperiodicity and Order* 59–110 (Elsevier Amsterdam, 1988).
98. Goldman, A. I. Magnetism in icosahedral quasicrystals current status and open questions. *STAM* **15**, 044801 (2014).
99. Andrade, E. C., Jagannathan, A., Miranda, E., Vojta, M. & Dobrosavljević, V. Non-fermi-liquid behavior in metallic quasicrystals with local magnetic moments. *Phys. Rev. Lett.* **115**, 036403 (2015).
100. Matsukawa, S., Deguchi, K., Imura, K., Ishimasa, T. & Sato, N. K. Pressure-driven quantum criticality and T/H scaling in the icosahedral Au–Al–Yb approximant. *J. Phys. Soc. Jpn.* **85**, 063706 (2016).
101. Shi, D. et al. Frustration and thermalization in an artificial magnetic quasicrystal. *Nat. Phys.* **14**, 309–314 (2018).
102. Edvardsson, S. & Klintonberg, M. Role of the electrostatic model in calculating rare-earth crystal-field parameters. *J. Alloy. Compd.* **275–277**, 230–233 (1998).

ACKNOWLEDGEMENTS

We thank Takanori Sugimoto and Taku J Sato for useful discussions. J.M.J. and S.B.L. were supported by National Research Foundation Grant (2021R1A2C109306013) and Nano Material Technology Development Program through the National Research Foundation of Korea(NRF) funded by Ministry of Science and ICT (RS-2023-00281839). This research was supported in part by grant NSF PHY-1748958 to the Kavli Institute for Theoretical Physics (KITP).

AUTHOR CONTRIBUTIONS

J.M.J. and S.B.L. develop main idea of the project. J.M.J. also produces the data and analyzes them. All authors contribute for writing the manuscript.

COMPETING INTERESTS

The authors declare no competing interests.

ADDITIONAL INFORMATION

Supplementary information The online version contains supplementary material available at <https://doi.org/10.1038/s41535-023-00617-z>.

Correspondence and requests for materials should be addressed to SungBin Lee.

Reprints and permission information is available at <http://www.nature.com/reprints>

Publisher's note Springer Nature remains neutral with regard to jurisdictional claims in published maps and institutional affiliations.



Open Access This article is licensed under a Creative Commons Attribution 4.0 International License, which permits use, sharing, adaptation, distribution and reproduction in any medium or format, as long as you give appropriate credit to the original author(s) and the source, provide a link to the Creative Commons license, and indicate if changes were made. The images or other third party material in this article are included in the article's Creative Commons license, unless indicated otherwise in a credit line to the material. If material is not included in the article's Creative Commons license and your intended use is not permitted by statutory regulation or exceeds the permitted use, you will need to obtain permission directly from the copyright holder. To view a copy of this license, visit <http://creativecommons.org/licenses/by/4.0/>.

© The Author(s) 2024